Mechanistic analysis of carbon–carbon bond formation by deoxypodophyllotoxin synthase

Haoyu Tang[a,1], Min-Hao Wu[b,1], Hsiao-Yu Lin[b], Meng-Ru Han[c], Yueh-Hua Tu[c], Zhi-Jie Yang[c], Tun-Cheng Chien[c,d,e,f,2], Nei-Li Chan[b,g,2], and Wei-chen Chang[a,2]

[a]Department of Chemistry, North Carolina State University, Raleigh, NC 27695; [b]Institute of Biochemistry and Molecular Biology, College of Medicine, National Taiwan University, Taipei 100, Taiwan; [c]Department of Chemistry, National Taiwan Normal University, Taipei 116, Taiwan; [d]Department of Medicinal and Applied Chemistry, Kaohsiung Medical University, Kaohsiung 807, Taiwan; [e]Faculty of Pharmacy, National Yang Ming Chiao Tung University, Taipei 112, Taiwan; [f]Department of Chemistry, Chung Yuan Christian University, Taoyuan 320, Taiwan; and [g]Life Science Group, National Synchrotron Radiation Research Center, Hsinchu 300, Taiwan

Edited by Wilfred van der Donk, Department of Chemistry, University of Illinois at Urbana–Champaign, Urbana, IL; received July 26, 2021; accepted November 22, 2021

Deoxypodophyllotoxin contains a core of four fused rings (A to D) with three consecutive chiral centers, the last being created by the attachment of a peripheral trimethoxyphenyl ring (E) to ring C. Previous studies have suggested that the iron(II)- and 2-oxoglutarate–dependent (Fe/2OG) oxygenase, deoxypodophyllotoxin synthase (DPS), catalyzes the oxidative coupling of ring B and ring E to form ring C and complete the tetracyclic core. Despite recent efforts to deploy DPS in the preparation of deoxypodophyllotoxin analogs, the mechanism underlying the regio- and stereoselectivity of this cyclization event has not been elucidated. Herein, we report 1) two structures of DPS in complex with 2OG and (±)-yatein, 2) in vitro analysis of enzymatic reactivity with substrate analogs, and 3) model reactions addressing DPS's catalytic mechanism. The results disfavor a prior proposal of on-pathway benzylic hydroxylation. Rather, the DPS-catalyzed cyclization likely proceeds by hydrogen atom abstraction from C7', oxidation of the benzylic radical to a carbocation, Friedel–Crafts-like ring closure, and rearomatization of ring B by C6 deprotonation. This mechanism adds to the known pathways for transformation of the carbon-centered radical in Fe/2OG enzymes and suggests what types of substrate modification are likely tolerable in DPS-catalyzed production of deoxypodophyllotoxin analogs.

C–C coupling | cyclization | oxygenase | natural product | reaction mechanism

Podophyllotoxin (**1**) and its congeners, including etoposide (**2**), teniposide (**3**), and etopophos (**4**), exhibit pronounced biological activities including antitumor, anti-HIV activity, antiviral, antimalarial, and antiasthmatic properties (Fig. 1) (1–5). Currently, **2**, **3**, and **4** are used as chemotherapeutic agents against small-cell lung cancer, acute leukemia, lymphoma, and testicular cancer (1–5). Podophyllotoxin-type compounds are characterized by a fused ring system (the A to D rings) with four chiral centers and a substituted benzene ring (the E ring). These unique structural features and resultant biological properties have drawn the interest of natural product and medicinal chemists. Recently, the genes required for podophyllotoxin biosynthesis were identified in *Sinopodophyllum hexandrum* (Himalayan mayapple) using a transcriptome mining approach. A pathway leading to (−)-4′-desmethylepipodophyllotoxin (5) (the aglycone of **2**, **3**, and **4**) was reconstituted in *Nicotiana benthamiana* (6). Previous studies have shown that an iron(II)- and 2-oxoglutarate–dependent (Fe/2OG) enzyme, deoxypodophyllotoxin synthase (DPS), is responsible for constructing the fused-ring system via coupling of aryl and benzylic carbons. In addition, DPS has been utilized as a biocatalyst for the preparation of podophyllotoxin and analogs through a chemoenzymatic approach (7, 8).

A key step in the formation of these secondary metabolites is the maturation of the fused-ring system through a regio- and stereospecific C–C bond formation in which (−)-yatein ((−)-**6a**) is converted to deoxypodophyllotoxin (**7a**) (Fig. 2). Based upon our current understanding of Fe/2OG enzymes, it was hypothesized that the conversion of **6a** to **7a** may proceed through a sequence of steps involving hydroxylation, dehydration to a quinonemethide-like oxonium intermediate, polar C–C coupling, and deprotonation to restore aromaticity (6). In vitro assays using substrate analogs, however, suggest that hydroxylation is less likely to be involved. Instead, a pathway including a radical or a cation driven C–C bond formation could be envisioned (Fig. 2) (8, 9). In both pathways, hydrogen atom abstraction is a common step to produce the substrate radical. In the latter pathway, instead of OH rebound, the interception of the resulting radical or cation by the B ring enables C–C bond formation. Other examples of natural products that are produced using a metalloenzyme to install key structural elements via C–C bond formation include complestatin, kainic acid, mycocyclosin, and rebeccamycin (10–17). Although metalloenzyme-catalyzed oxidative C–C bond-forming reactions appear to be a commonly used strategy to expand structural complexity in natural products, the underlying mechanisms, including the pathway leading to deoxypodophyllotoxin

Significance

The completion of the tetracyclic core of etoposide, classified by the World Health Organization as an essential medicine, by the Fe/2OG oxygenase deoxypodophyllotoxin synthase follows a hybrid radical-polar pathway not previously seen in other members of this enzyme class. The implication of a substrate-based benzylic carbocation in this mechanism will inform ongoing efforts to create analogs of this important drug with improved or emergent properties and represents a new route for resolution of the initial substrate radical that is common to members of the class. This study adds to our understanding on a growing number of biochemical transformations in which carbocation intermediates are likely to be crucial.

Author contributions: H.T., M.-H.W., H.-Y.L., M.-R.H., Y.-H.T., Z.-J.Y., T.-C.C., N.-L.C., and W.-c.C. designed research; H.T., M.-H.W., H.-Y.L., M.-R.H., Y.-H.T., Z.-J.Y., T.-C.C., N.-L.C., and W.-c.C. performed research; H.-Y.L. and W.-c.C. contributed new reagents/analytic tools; H.T., M.-H.W., Y.-H.T., Z.-J.Y., T.-C.C., N.-L.C., and W.-c.C. analyzed data; and H.T., M.-H.W., T.-C.C., N.-L.C., and W.-c.C. wrote the paper.

The authors declare no competing interest.

This article is a PNAS Direct Submission.

[1]H.T. and M.-H.W. contributed equally to this work.

[2]To whom correspondence may be addressed. Email: tcchien@ntnu.edu.tw, nlchan@ntu.edu.tw, or wchang6@ncsu.edu.

This article contains supporting information online at http://www.pnas.org/lookup/suppl/doi:10.1073/pnas.2113770119/-/DCSupplemental.

Published December 28, 2021.

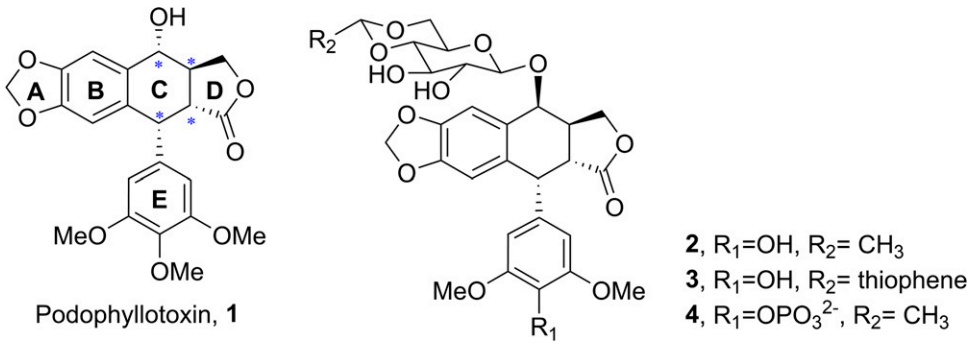

Fig. 1. Structure of podophyllotoxin (**1**), etoposide (**2**), teniposide (**3**), and etopophos (**4**). Asterisk (*) labels represent the chiral centers.

formation, remain underexplored. To gain structural insight into the pathways involved in 1) the generation of the podophyllotoxin core specifically and 2) oxidative C–C-coupling reactions in general, we solved the structures of DPS in complex with (±)-**6a** and 2OG. Furthermore, we employed mechanistic probes and model reactions to investigate the reaction mechanism of the DPS-catalyzed cyclization. Instead of proceeding via benzylic hydroxylation, we have found that a pathway involving a carbocation is likely utilized to affect **7a** formation.

Results and Discussion

Crystal Structures of Substrate- and 2OG-Bound DPS. To provide insight into DPS catalysis, DPS structures were solved in the presence of the substrate (DPS•Fe•succinate•(±)-**6a**) and 2OG (DPS•Fe•2OG) at resolutions of 2.05 and 2.09 Å, respectively (Fig. 3 *A* and *B* and *SI Appendix*, Fig. 1 and Table 1; Protein Data Bank identification code: 7E37 and 7E38). The structure of DPS•Fe•succinate•(±)-**6a** was initially solved by two-wavelength anomalous diffraction (MAD) at 2.45 Å resolution using datasets collected from a single selenomethionine-labeled protein crystal followed by phase extension to 2.05 Å resolution using a higher-quality native dataset. The DPS•Fe•2OG structure was then solved by molecular replacement.

Similar to other members of the Fe/2OG enzyme superfamily (18), DPS adopts a double-stranded β-helix (DSBH) fold with a β-barrel core composed of eight strands arranged in jellyroll topology (*SI Appendix*, Fig. 1*B*). The active site of DPS consists of a 2-His-1-carboxylate facial triad (formed by His184, Asp186, and His239) for iron coordination, an RXS motif (composed of Arg249 and Ser251), a nearby Tyr169 for 2OG binding, and several residues with differential polarity that enable substrate positioning (Fig. 3 *C* and *D*). The iron in the DPS•Fe•2OG ternary structure is octahedrally coordinated by the side chains of the facial triad residues, bidentate ligation of the α-keto acid moiety of 2OG, and one water molecule. Notably, Fe-ligated 2OG exhibits an offline-binding mode in which the carboxylate group of 2OG is positioned *trans* to the distal histidine (His239) (Fig. 3*C* and *SI Appendix*, Figs. 2*A* and 3) (18–23). Given that the coordinated water likely reflects the position of the reactive iron–oxo group, we speculate that a rearrangement of the presumptive iron–oxo species may take place during the reaction.

Structural Analysis Reveals Plausible Cyclization Pathways. Substrate-bound DPS crystals were produced by cocrystallization with the substrate (±)-yatein ((−)-**6a** and its enantiomer (+)-**6a** in which the (+) and (−) signs reflect the rotation direction in the polarimeter). The experimental MAD-phased electron density map of DPS•Fe•succinate•(±)-**6a** is of sufficient quality to allow the three cyclic moieties of yatein, the benzodioxole bicyclic ring (the A and B rings), the lactone ring (the D ring), and the phenyl ring (the E ring), to be placed unambiguously in the active site (*SI Appendix*, Fig. 4). Automated ligand fitting by Coot revealed that both (−)- and (+)-**6a** can be docked readily (Fig. 3 *E* and *F*) (24), suggesting that (−)- and (+)-**6a** may coexist in the crystals. Therefore, both enantiomers were built into the structure and refined with partial occupancy. Despite the chirality difference of the lactone ring (the D ring), both enantiomers adopt a U-shaped conformation and have similar interactions with surrounding amino acid residues (*SI Appendix*, Fig. 5). The benzodioxole moiety (the A and B rings) forms a face-to-face π–π interaction with His165 and has van der Waals interactions with Thr86, Met167, Leu181, and Phe290. In addition, it lies parallel to the polar surface formed by four main-chain carbonyl oxygen atoms (residues Pro80, Glu81, Tyr82, and Gly84) and a nearby water molecule (Fig. 4 *A*–*C*). The lactone ring (the D ring) is sandwiched by the side chains of Phe255 and Phe290 and is in close proximity with Phe257 and Leu286 (Fig. 4*D*). In addition, a buried hydrogen bond is present between the carbonyl oxygen of the lactone and the main-chain amide nitrogen of Lys187. The phenyl ring (the E ring) is located in a spatially restricted hydrophobic crevice created by Leu181, His184, Lys187, Phe290, and Val298. A hydrogen bond between the *para*-methoxy group of the E ring and a water molecule was also observed. In addition, π–π stacking between the E ring and the imidazole of the proximal histidine (His184) indicates that the 2-His-1-carboxylate facial triad may contribute to substrate recognition beyond its canonical role in Fe coordination (Fig. 4*E*). The highly comparable binding modes observed for (−)- and (+)-**6a** are consistent with the reported observation that both enantiomers can be used as substrates (8). Notably, compared with the 2OG-bound structure (DPS•Fe•2OG), the substrate-bound structure (DPS•Fe•succinate•(±)-**6a**) clearly shows that succinate is located at a deeper position than the substrate in the active site (*SI Appendix*, Fig. 2*B*). Assuming that 2OG and succinate bind at a similar position in the active site, this observation implies that 2OG and the substrate likely enter the active site sequentially.

The adoption of a U-shaped conformation by **6a** in the active site hints at possible pathways for C–C bond formation (Fig. 5 *A* and *B*). Specifically, the observed orientation of the benzodioxole moiety with respect to the phenyl ring places C6 of the B ring and C7′ of the E ring in close proximity. The distance between C6 and C7′ in the active site is ∼3.5 Å for both (−)-**6a** and (+)-**6a**, which accurately predicts the position and the stereo-preference of the resulting C6–C7′ bond (Fig. 5 *A* and *B*). Moreover, the benzylic carbon (C7′) of the E ring in (−)- and (+)-**6a** is positioned close to the iron center with an Fe–C distance of 3.9 and 4.4 Å, respectively. In this position, the C7′–H is poised for hydrogen atom abstraction. By contrast, the C6 carbon has Fe–C distances of 5.7 and 5.9 Å that is inappropriate to serve in this capacity without significant

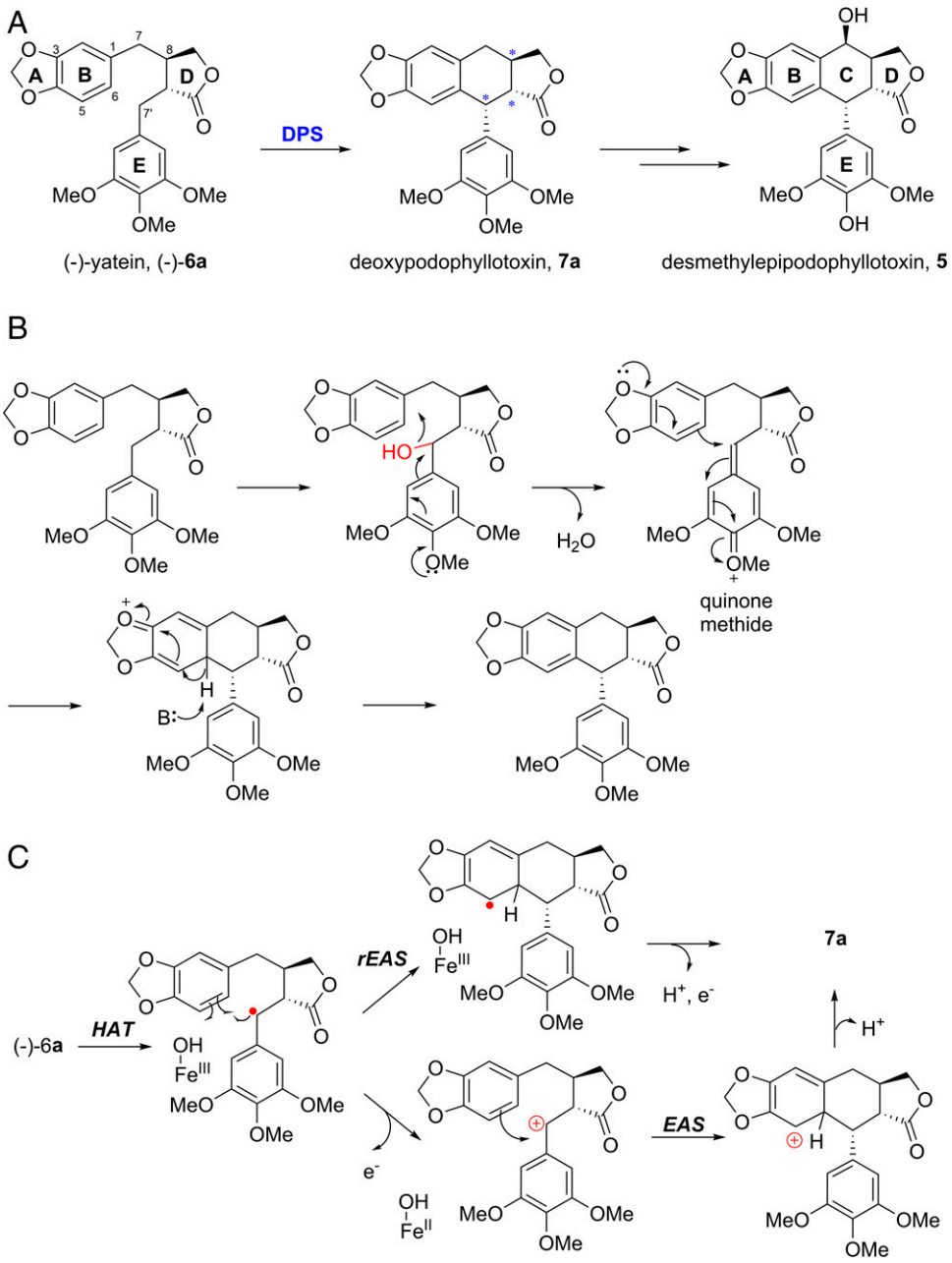

Fig. 2. (*A*) DPS catalyzes the conversion of (−)-yatein (**6a**) to deoxypodophyllotoxin (**7a**), which serves as the key intermediate in (−)-4′-desmethylepipodophyllotoxin (**5**) biosynthesis. (*B*) On the basis of current understanding of Fe/2OG enzyme catalysis, a possible mechanism accounting for **7a** production is proposed. Following hydroxylation, the resulting quinone methide intermediate triggers C–C bond formation. Subsequent deprotonation restores the aromaticity and furnishes **7a**. (*C*) Through in vitro assays using substrate analogs (8, 9), instead of OH rebound, pathways that include a radical electrophilic aromatic substitution (rEAS) or an electrophilic aromatic substitution (EAS) are also conceivable (46).

reorientation. Notably, due to the offline binding of 2OG observed in the DPS•Fe•2OG structure, rearrangement of the iron–oxo species is anticipated to enable hydrogen atom abstraction at C7′ (*SI Appendix*, Fig. 3) (20, 22, 23).

These observations suggest that the primary hydrogen atom abstraction site is at C7′, which is consistent with previous results from in vitro assays (9). Moreover, given that the D and E rings of the substrate are anchored tightly in the active site (Fig. 4 *D* and *E*), formation of the C–C bond is likely enabled through rotation of the benzodioxole moiety, which brings C6 toward C7′ (Fig. 5 *A* and *B*). To elucidate the stereochemistry and the plausible factors that govern this reaction, we performed manual docking of the reaction products (**7a** and **8a**, Fig. 6*A*) and their corresponding C7′ epimers into the active site assuming that the lactone ring occupies the same binding pocket as the substrate ((±)-**6a**). The resulting chirality of C6 and C7′ of the predicted product generated by swinging the AB ring toward the E ring matches those of **7a** and **8a**. In contrast, without relocating the D ring, the formation of the product with the opposite chirality at C7′ would inflict severe steric clashes of the E ring with the iron and the iron-ligating residues (Fig. 5 *C* and *D*).

Reconstitution of the DPS Reactivity In Vitro and Product Characterization. The substrate-bound DPS structure reveals the primary hydrogen atom abstraction site as well as the stereospecificity of the DPS-catalyzed reactions. To elucidate the

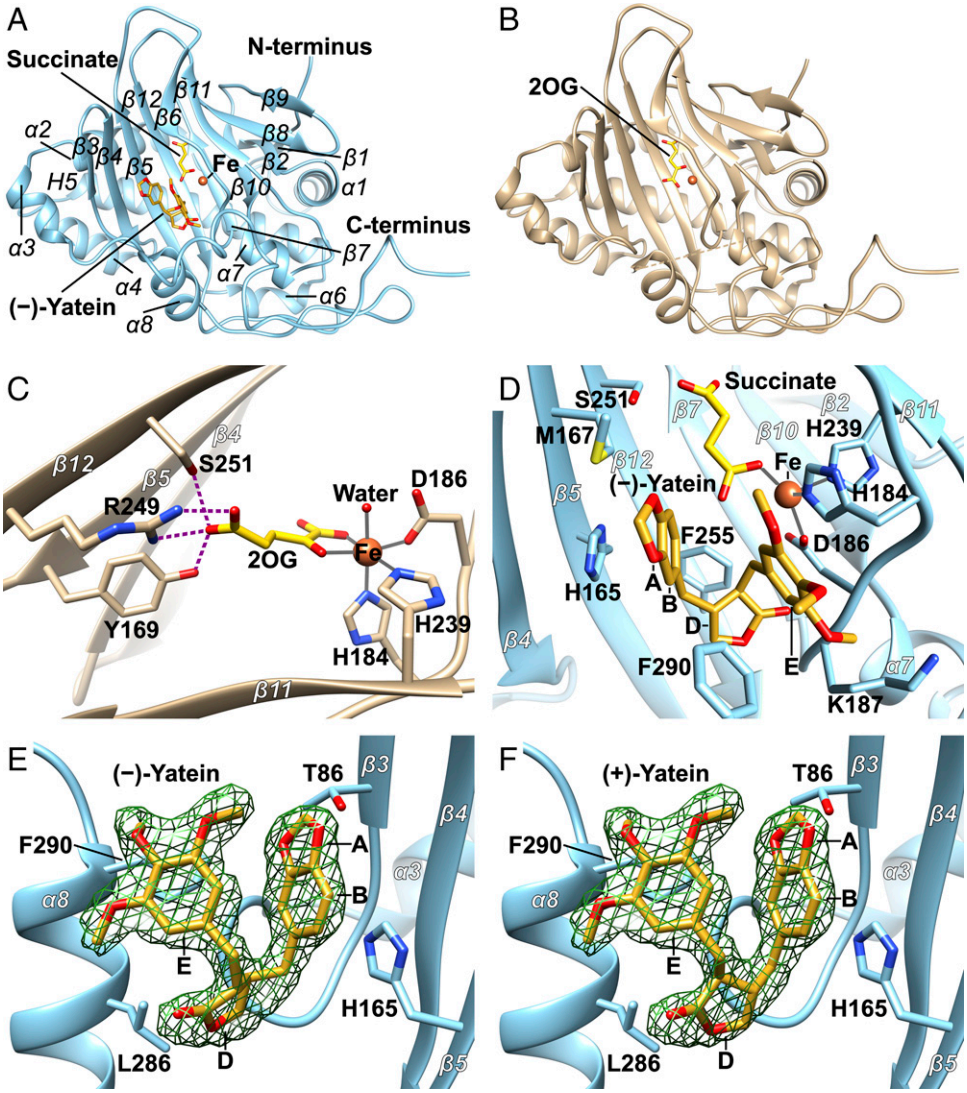

Fig. 3. Structures of DPS in complexes with yatein and cofactors. (*A*) Overall structure of the DPS•Fe•succinate•(±)-**6a** quaternary complex (Protein Data Bank identification: 7E38). DPS is composed of eight α-helices (α1 to α8) and twelve β-strands (β1 to β12) in which strands β5 through β12 adopt the double-stranded β-helix architecture. The substrate (−)-**6a** and the coproduct succinate are shown in stick representation, and the catalytic iron is shown as an orange sphere. (*B*) Overall structure of the DPS•Fe•2OG ternary complex (Protein Data Bank identification: 7E37). The cofactor 2OG is shown in sticks, and the eight residues (292 to 299) missing in this structure are represented as dashed lines. (*C* and *D*) Structure of the DPS active site. Residues responsible for 2OG binding and iron coordination, according to the DPS•Fe•2OG ternary complex, are shown in *C*. Residues responsible for substrate and coproduct (succinate) binding and iron coordination, as observed in the DPS•Fe•succinate•(±)-**6a** quaternary complex, are shown in *D*. The coordination bonds formed by iron are presented as solid lines (gray); hydrogen bonds are presented as dashed lines (magenta). For clarity of visualization, only (−)-**6a** is displayed. (*E* and *F*) Electron density map of the DPS-bound substrate. Unbiased mF_o-DF_c electron density map of the substrate contoured at 3σ (green mesh) fitted with (−)-**6a** (*E*) and (+)-**6a** (*F*).

reaction pathway, we carried out the DPS-catalyzed cyclization reaction in vitro on the native substrate (−)-**6a** to produce the desired product **7a**. The reaction involved mixing 1 mM (−)-**6a** and 2.5 mM 2OG with 250 μM reconstituted DPS in 100 mM Tris buffer (pH 7.5) at 4 °C. After incubation, the enzyme was precipitated using an equal volume of acetonitrile and centrifuged. The solution was then analyzed by high-performance liquid chromatography coupled mass spectrometry (HPLC-MS) using a C18 analytical column. As shown in Fig. 6*B*, consumption of the substrate with concomitant formation of a new product was detected. The peak of the new product has an *m*/*z* value of 421.1 (electrospray ionization in positive mode), which corresponds to the predicted product **7a**. When a racemic mixture containing (−)-**6a** and (+)-**6a** ((±)-**6a**) was used, two peaks with the same *m*/*z* values were observed. This result suggests that two cyclized products, for example, **7a** and **8a**, are produced at the expense of (±)-**6a**. The second peak coeluted with the product generated using (−)-**6a** as the substrate. Interestingly, production of a peak which has an *m*/*z* value consistent with hydroxylation (*m*/*z* = 439.1) was also detected when DPS was incubated with (±)-**6a** but not with (−)-**6a**. NMR and polarimetric analysis of a large-scale DPS reaction using (±)-**6a** revealed that the isolated products are deoxypodophyllotoxin (**7a**), the corresponding isomer which has the opposite stereochemistry of the D ring (**8a**) and the C7′ hydroxylation product (**9a**) (Fig. 6*A*). In both **7a** and **8a**, the stereochemical configuration of C7′ retains an *R* configuration with H7′–H8′ coupling constants of 2.6 and 11 Hz, respectively. In **7a**, a coupling constant of 2.6 Hz indicates that the two vicinal protons at C7′ and C8′ are oriented toward the same face. In contrast, a coupling

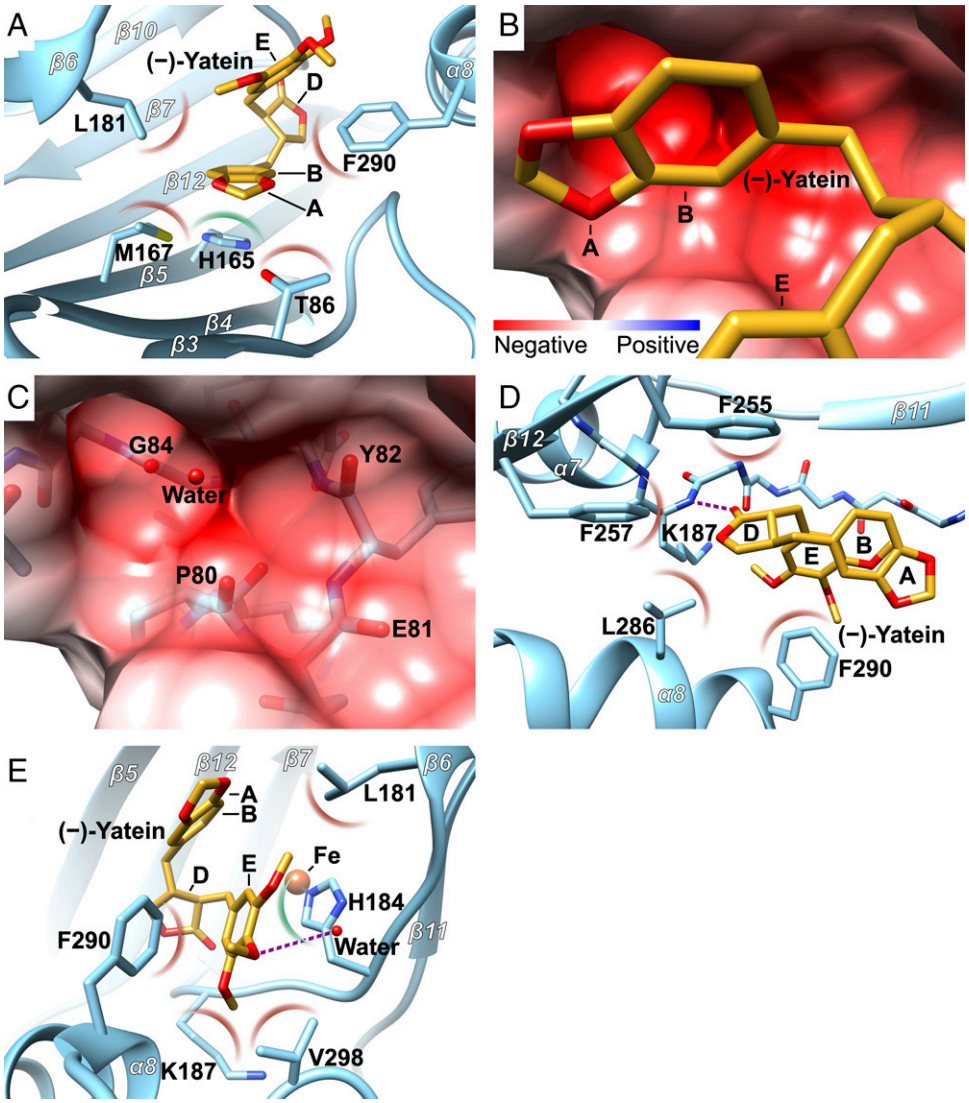

Fig. 4. Structural basis of substrate recognition by DPS. (*A*) Interactions between DPS and the AB ring (benzodioxole moiety) of (±)-**6a**. (*B*) The electrostatic potential surface displayed for the pocket surrounding the AB ring of (±)-**6a** reveals that the surface is partially negatively charged due to the presence of several exposed main-chain carbonyl oxygen atoms. (*C*) Composition of the amino acid residues shown in *B*. For clarity, (−)-**6a** is omitted, and residues of DPS are shown as sticks. (*D*) Interactions between DPS and the D ring (the lactone ring) of (±)-**6a**. (*E*) Interactions between DPS and the E ring of (±)-**6a**. The color and labeling follow those used in Fig. 3 with the selected DPS residues in blue sticks. Van der Waals interactions and π–π interactions are represented by maroon and green arcs, respectively. Only one enantiomer ((−)-**6a**) is displayed for clarity of visualization.

constant of 11 Hz suggests a diaxial arrangement of H7′–H8′ in **8a**. The NMR spectrum of **9a** is consistent with the NMR spectrum of *epi*-podorhizol; however, it has a similar but opposite specific rotation as *epi*-podorhizol (+25.5, $[\alpha]_D^{22}$, $CHCl_3$, c = 0.72 versus −20.8, $[\alpha]_D^{23}$, CH_2Cl_2-hexanes and −32.6, $[\alpha]_D^{23}$, $CHCl_3$, c = 0.62) (25, 26). Thus, **9a** is characterized as the enantiomer of *epi*-podorhizol. Formation of **9a** implies that one of the following scenarios is conceivable for the reaction with the enantiomeric substrate ((+)-**6a**): 1) hydroxyl rebound competes more effectively with electron transfer as a result of acceleration of the former step and/or retardation of the latter, or 2) the coupling of the C7' carbocation to C6 is impeded, allowing it to be quenched by solvent. As shown in previous work on Fe/2OG halogenases, subtle differences in substrate positioning can alter reaction outcomes in this fashion (27–30). These results demonstrate that the DPS-catalyzed C–C bond-forming reaction using both (−)-yatein and (+)-yatein retains stereoselectivity regardless of the chirality of the D ring. The C7′ atom has an *R* configuration in both **7a** and **8a**, and is in accordance with the crystal structure observation in which the active site imposes constraints on the D and E rings of the substrate to enable stereoselective C–C bond formation.

Using Analogs to Elucidate the Mechanism of the DPS-Catalyzed C–C Bond Formation. In the previously proposed mechanism (6), a lone pair of the *para*-methoxy group is used to enable formation of the quinone methide intermediate through removal of a hydroxyl group that is installed via OH rebound. The quinone methide intermediate then triggers C–C bond formation (Fig. 2*B*). In this scenario, replacement of the methoxy group with other moieties that disable quinone methide formation should prevent/impede C–C bond formation and possibly redirect the reaction. Chemically synthesized substrate analogs where the methoxy group was replaced with a proton or a methyl group ((±)-**6b** and (±)-**6c**) were used as mechanistic probes to test this hypothesis. When (±)-**6b** and (±)-**6c** were incubated with DPS, the enzymatic products showed mass signals that matched cyclized products. Further NMR and polarimetric analysis

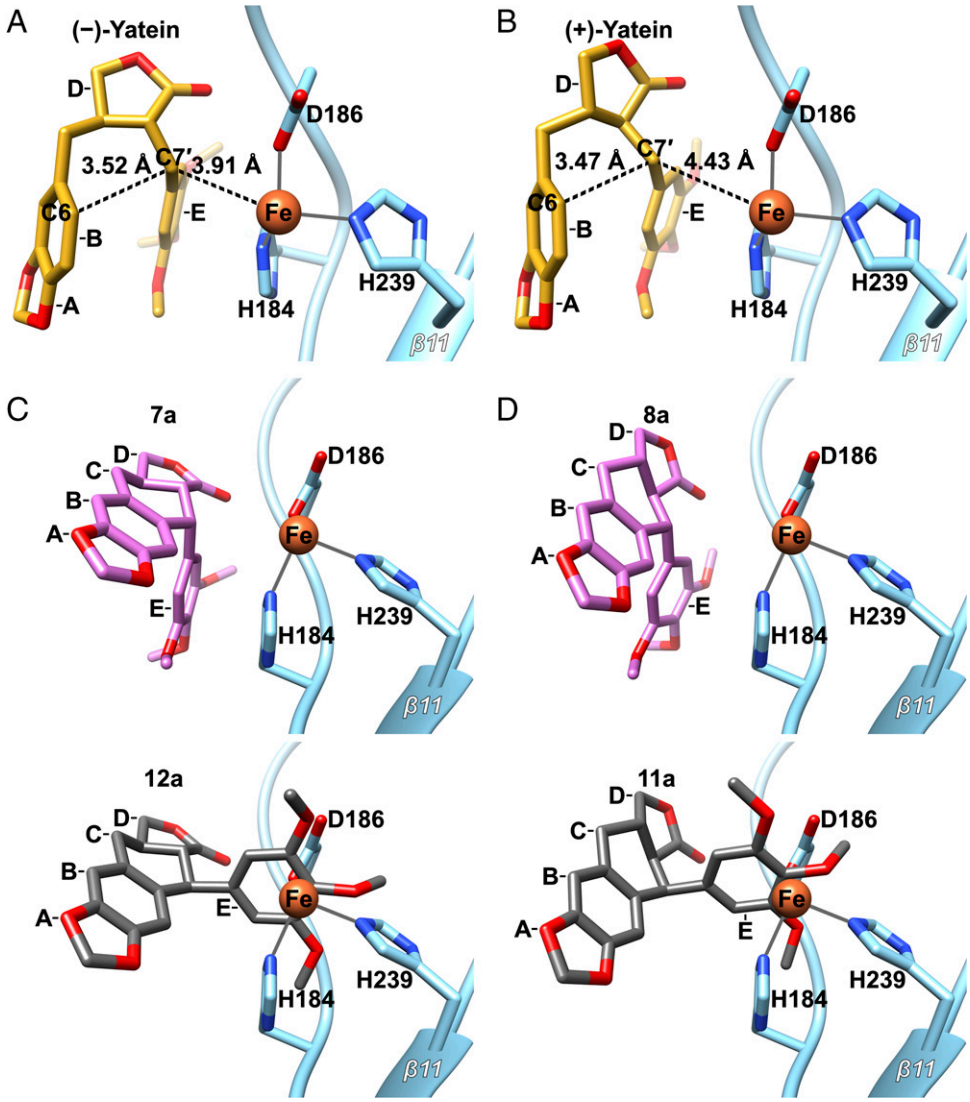

Fig. 5. Yatein-binding mode observed in the DPS active site ensures the generation of regiospecific products. (*A* and *B*) Distances are shown between C6–C7′ and C7′–iron in DPS-bound (−)-**6a** (*A*) and (+)-**6a** (*B*). (*C* and *D*) The formation of **7a** (*C*, *Upper*) and **8a** (*D*, *Upper*) (purple sticks) can be readily achieved by swinging the AB ring toward C7′ without relocating the lactone ring and E ring in the binding pocket. In contrast, due to steric conflicts with the iron and the iron-ligating residues, formation of the C7′ epimers of **7a** and **8a** (**12a** and **11a**, shown as gray sticks in *Bottom* of *C* and *D*, respectively) is disfavored.

confirmed that the reaction products are deoxypodophyllotoxin analogs and the corresponding isomers that have the opposite stereochemistry of the D ring (**7b**/**7c** and **8b**/**8c**). These findings strongly suggest that a quinone methide is not required for C–C bond formation. Therefore, a distinct reaction pathway, that is, a radical or a cation-induced C–C bond formation, which does not involve quinone methide, should be considered.

To delineate the role of the *para*-substituent of the E ring in the DPS-catalyzed reaction, steady-state kinetics were measured in duplicate over a concentration range of (±)-**6a** (100 to 500 μM) in the presence of 1 μM reconstituted DPS and 1 mM 2OG in 100 mM Tris buffer (pH 7.6) at room temperature. The analogous experiments were also carried out using (±)-**6b** and (±)-**6c** (*SI Appendix*, Fig. 6). The Michaelis constants (K_M) for (±)-**6a**, **6b**, and **6c** are 0.23, 0.05, and 0.13 mM. The resulting k_{cat}/K_M values for (±)-**6a**, **6b**, and **6c** are 11.7, 1.6, and 5.1 $mM^{-1} \cdot min^{-1}$, respectively. In comparison with **6b**, a ∼7.2- and 3.2-fold increase in catalytic efficiency (k_{cat}/K_M) for **6a** and **6c** is possibly associated with the electron-donating properties of the methoxy and methyl groups. In addition, the smaller K_M value for **6b** likely reflects the steric effect of the *para*-substituent of the E ring. On the other hand, it is possible that changing substituents on the substrate in enzyme catalysis may simultaneously alter several kinetic parameters.

To further explore the reaction mechanism, the hydroxylation product (**9a**) isolated from the large-scale reaction was incubated with DPS. Even after 20 h incubation, neither substrate consumption nor product formation was observed by HPLC-MS (*SI Appendix*, Fig. 7). Although we cannot rule out the possibility of nonoptimal binding of **9a** that prevents C–C bond formation, this observation is in accordance with the results obtained using substrate analogs (**6b** and **6c**) and further suggests that quinone methide is unlikely to be involved in the DPS reaction.

Biomimetic Chemical Model Studies Reveal the Chemical Rationale of DPS Catalysis. Based on the substrate-bound DPS structure, in vitro results, and detailed product structural characterization, it is unlikely that the DPS reaction proceeds through a pathway involving hydroxylation and a quinone methide intermediate. To gain insight into the chemistry of this reaction, chemically

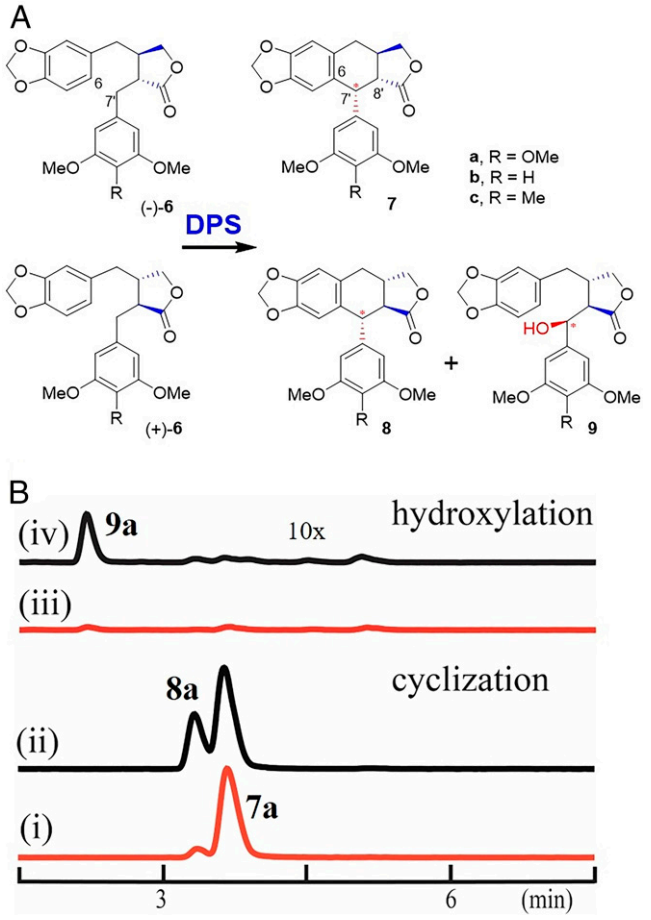

Fig. 6. (*A*) Products generated by DPS from various substrate analogs. Regardless of the stereochemical configuration of the D ring, DPS catalyzes stereospecific C–C bond formation. Substrate (−)-**6a** is converted to **7a**. In the case of (±)-**6a**, in addition to **7a** and **8a**, the hydroxylation product (**9a**) is also generated. Asterisks (*) denote newly generated chiral center. (*B*) HPLC-MS chromatograms of the DPS-catalyzed reactions. For (−)-**6a**, only the cyclized product **7a** is produced (traces i and iii). When (±)-**6a** is used as the substrate, cyclization products (**7a** and **8a**) and the hydroxylation product (**9a**) are detected (traces ii and iv). The traces iii and iv are magnified by 10-fold for visualization.

synthesized (±)-**10a** and **10b** were subjected to a reaction containing trifluoroacetic acid in dichloromethane. The consumption of substrates (**10a** and **10b**) with concomitant formation of new products were detected by thin-layer chromatography and NMR spectroscopy. The structures of the isolated products were determined by NMR and X-ray analyses (*SI Appendix*, Figs. 42–46, Tables 2–5). For (±)-**10a**, two pairs of enantiomers, **7a**/**11a** and **8a**/**12a**, were obtained with an isolated yield of 96% (1% of **7a**/**11a** and 95% of **8a**/**12a**). In contrast, substrate (±)-**10b** exhibits much lower reactivity. After a prolonged reaction time (i.e., 14 d versus 4 h in (±)-**10a**), **7b**/**11b** and **8b**/**12b** were obtained in 19% yield (6% of **7b**/**11b** and 13% of **8b**/**12b**, Fig. 7). In addition, a trace amount of **13b** was produced. Notably, we did not observe the corresponding desaturation product using (±)-**10a**. The formation of the cyclized products using **10b** indirectly supports that the reaction pathway does not involve a quinone methide intermediate. Furthermore, production of both **7**/**11** and **8**/**12** suggests that C–C bond formation is not stereospecific under chemical conditions. Therefore, the stereoselectivity observed in the DPS-catalyzed reactions is most likely enabled by the spatial orientation of the substrate within the enzyme active site.

As suggested in the previous studies (31–34), the trifluoroacetic acid-promoted formation of deoxypodophyllotoxin using **10a** and **10b** most likely proceeds through formation of a benzylic carbocation. The reaction is then followed by an intramolecular Friedel–Crafts-type alkylation and deprotonation to restore aromaticity. In comparison with **10a**, generation of the carbocation in **10b** is less favored, which is consistent with lower product yield and prolonged reaction time required for efficient product formation. Importantly, this observation is in accordance with the in vitro assay in which the catalytic efficiency of (±)-**6a** is ∼7.2-fold of (±)-**6b**. Even though the pathway leading to carbocation formation in the model studies includes an acid-assisted dehydration which is different from enzymatic catalysis, the influence of the *para*-substituent at the E ring suggests that both model studies and the DPS-catalyzed reaction may utilize a similar intermediate to facilitate the C–C bond formation.

Conclusion

Since the recent discovery of C–C bond-forming reactions catalyzed by Fe/2OG enzymes, these proteins have been utilized in the preparation of podophyllotoxins and kainic acid through chemoenzymatic cascades. The mechanism of these chemically challenging reactions, however, remains to be elucidated. An analysis of the substrate- and 2OG-bound protein structures suggest that substrate positioning could be the primary determinant in the DPS-catalyzed C−C bond-forming reaction. First, the U-shaped configuration of both (−)- and (+)-**6a** in the active site clearly indicates the primary hydrogen abstraction site is at C7′ of the E ring. Second, the active site imposes constraints on the D and E rings to facilitate the regio- and stereoselective formation of the C–C bond. The in vitro assay results using the substrate **6a** and its analogs (**6b** and **6c**) demonstrate that DPS is promiscuous toward the chirality of the D ring and the *para*-substituent of the E ring. In addition, the opposite configuration at C7′ of **8a** and **9a** suggests that hydroxylation is likely a side product and not the on-pathway intermediate. The production of the corresponding cyclized products, that is, **7b**/**7c** and **8b**/**8c**, weigh against the function of the *para*-methoxy group as enabling quinone methide intermediate formation: in this case, replacement of the methoxy group with a methyl group or a proton ought to have prevented quinone methide intermediate to disable C–C bond formation. Notably, the influence of the *para*-substituent toward catalytic efficiency is in accordance with the involvement of a carbocation.

The verification of these observations using model studies provides a chemical rationale for the DPS-catalyzed reactions. The formation of cyclized product using **10b** suggests that the formation of quinone methide is not required for C–C bond formation. Furthermore, there is a correlation between the electron-donating property of the *para*-substituent and the product yield in accordance with the involvement of a carbocation intermediate. It is worth noting that the model reactions and the enzymatic reactions were carried out under different conditions, for example, pH and solvent, which may influence the reaction pathway. The model studies further imply that the stereoselectivity observed in the DPS reaction is enabled through the conformation of the substrate in the active site.

In summary, our substrate-bound DPS structure demonstrates the importance of substrate positioning and delineates the most likely reaction pathway as illustrated in Fig. 8. Upon entering the active site, the conformational change of the substrate enables hydrogen atom abstraction to occur at the pro*R* hydrogen of C7′. Rather than undergoing hydroxyl rebound, a pathway including a carbocation-induced C–C bond formation is likely to be utilized. The active site imposes constraints on the D and E rings to enable regio- and stereo-selective cyclization. Deprotonation restores aromaticity and completes the reaction. Notably, this reaction is

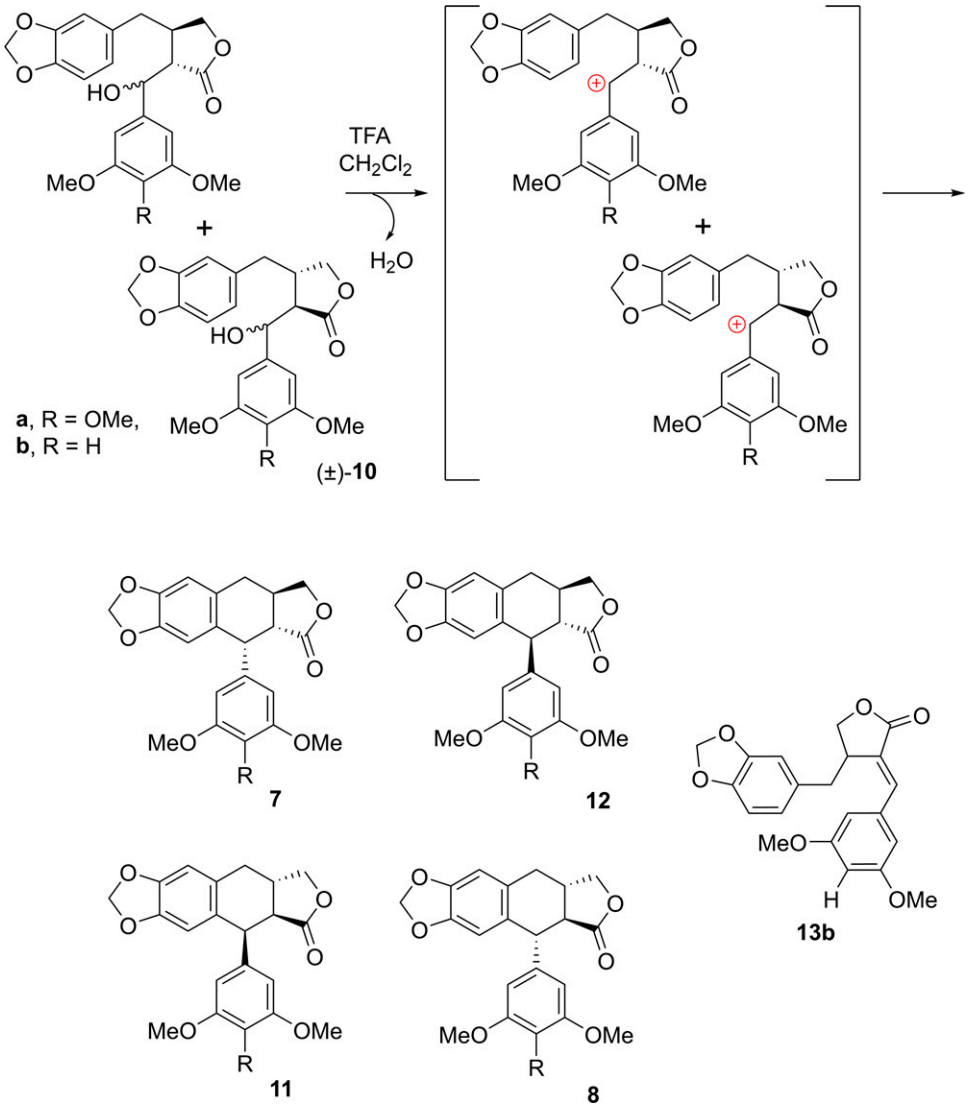

Fig. 7. Chemical model studies on the synthesis of deoxypodophyllotoxin analogs. (±)-**10a** and **10b** are converted to **7**/**11** and **8**/**12**. Under current reaction conditions, the cyclization most likely proceeds through a Friedel–Crafts alkylation mechanism. A carbocation generated via trifluoroacetic acid-assisted dehydration serves as the key intermediate to trigger C–C bond formation.

catalytic, and thus, the iron returns to Fe(II) at the end of the reaction. This mechanistic hypothesis is also consistent with the reduced catalytic efficiency and product yields using substrate analogs in the biochemical assays and in the chemical model studies. Taken together, these results provide the experimental insight and chemical rationale that underpin a plausible reaction pathway for C–C bond formation and add to a growing number of biochemical transformations in which carbocation intermediates are likely to be crucial (35, 36). Along with hydroxylation, halogenation, and other recently identified transformations, including desaturation, endoperoxidation, isocyanide formation, and stereoinversion (18, 20, 37–45), these findings serve to highlight the mechanistic subtleties of Fe/2OG enzymes associated with natural product biosynthesis.

Materials and Methods

Detailed materials and methods are provided in *SI Appendix*. The protein structures (7E37 and 7E38) have been deposited to the Protein Data Bank.

X-ray Crystallographic Characterization. C-terminally His_6-tagged DPS was overexpressed and purified as detailed in *SI Appendix*. The DPS•Fe•2OG ternary complex was crystalized by mixing 1 μL protein sample (0.3 mM DPS, 0.45 mM $FeCl_2$, and 0.6 mM 2OG) with an equal volume of reservoir solution (0.1 M Tris HCl pH 8.5, 0.2 M lithium sulfate, and 25% wt/vol polyethylene glycol (PEG) 3,350) and then equilibrated against 200 μL reservoir solution at 4 °C. For the DPS•Fe•succinate•(±)-yatein complex, crystals were obtained by mixing 0.15 μL protein sample (0.28 mM DPS, 0.42 mM $FeCl_2$, 0.55 mM succinate, and 0.55 mM (±)-yatein) with 0.15 μL reservoir solution (0.1 M Hepes pH 7.5 and 1.4 M sodium citrate) and 0.3 μL size-exclusion chromatography buffer (25 mM Tris HCl pH 7.5, 150 mM NaCl, and 2 mM 2-mercaptoethanol) and equilibrating against 20 μL reservoir solution at 4 °C. Data collection and refinement procedures are described in *SI Appendix*.

Characterization of the DPS-Catalyzed Reaction. In vitro assays and the large-scale enzymatic synthesis were carried out in Tris HCl buffer. After mixing the substrate, reconstituted enzyme, and 2OG, the reaction mixture was exposed to air. The reactions were quenched by adding acetonitrile to the reaction mixtures, and samples were analyzed by HPLC-MS. Detailed procedures and product structure characterization are described in *SI Appendix*.

Chemical Model Studies. Chemical model studies were carried out in dichloromethane. To a solution that contains (±)-**10a** or (±)-**10b** was added trifluoroacetic acid (TFA) at 0 °C. The reaction was warmed to room temperature, and the progress was monitored using thin-layer chromatography (TLC). The substrate and analogs syntheses and product structural characterizations are described in *SI Appendix*.

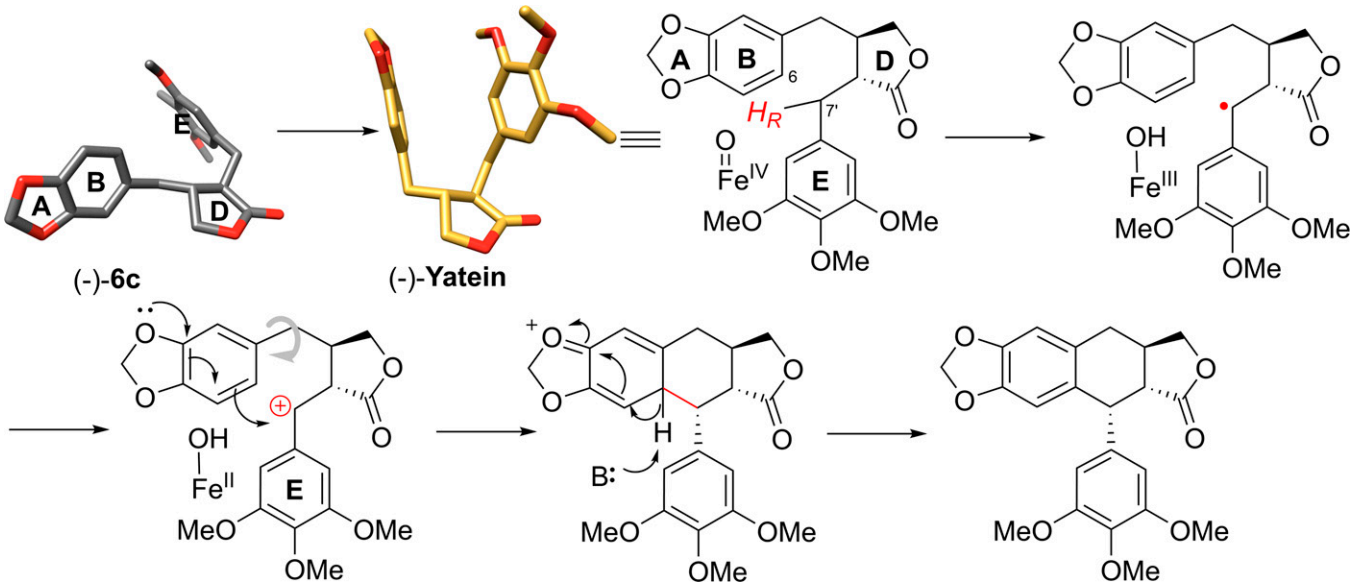

Fig. 8. Proposed mechanism of DPS-catalyzed deoxypodophyllotoxin formation. Upon entering the active site, the substrate adopts a U-shaped conformation (Fig. 3 *E* and *F*), which poises the pro*R* hydrogen at C7′ for hydrogen atom abstraction. As suggested by the substrate-bound DPS structure, the D and E rings of the substrate are anchored tightly in the active site (Fig. 4 *D* and *E*), and C–C bond formation is likely to be enabled through rotation of the benzodioxole moiety (the A and B rings), which brings C6 toward C7′ carbocation. Subsequent to C–C bond formation, deprotonation at C6 restores the aromaticity of the B ring. Based on the in vitro assay results using substrate analogs, hydroxylation is unlikely to be involved in the DPS-catalyzed C–C bond formation.

Data Availability. All study data are included in the article and/or *SI Appendix*. The protein structures (accession numbers 7E37 and 7E38) have been deposited to the Protein Data Bank.

ACKNOWLEDGMENTS. This work was supported by the NSF (Grant CHE-1845913 to W.-c.C.), Ministry of Science and Technology, Taiwan (Grants 109-2113-M-002-006, 109-2326-B-002-008, and 107-2923-B-002-001-MY4 to N.-L.C. and 109-2113-M-003-005 to T.-C.C.), North Carolina State University, National Taiwan Normal University, and National Taiwan University (NTU-110 L893405 to N.-L.C.). Portions of this research were carried out at beamlines Taiwan Light Source 15A1 and Taiwan Photon Source 05A1 of the National Synchrotron Radiation Research Center (Taiwan). We are grateful to the staff of Technology Commons in the College of Life Science and Center for Systems Biology, National Taiwan University. We also thank Drs. Chih-Chiang Chang and Ying-Ren Wang for helpful discussions.

1. R. Canetta, P. Hilgard, S. Florentine, P. Bedogni, L. Lenaz, Current development of podophyllotoxins. *Cancer Chemother. Pharmacol.* **7**, 93–98 (1982).
2. S. Joel, The clinical pharmacology of etoposide: An update. *Cancer Treat. Rev.* **22**, 179–221 (1996).
3. F. A. Greco, J. D. Hainsworth, Clinical studies with etoposide phosphate. *Semin. Oncol.* **23**, 45–50 (1996).
4. Y. Q. Liu *et al.*, Recent progress on C-4-modified podophyllotoxin analogs as potent antitumor agents. *Med. Res. Rev.* **35**, 1–62 (2015).
5. World Health Organization, *Model List of Essential Medicines, 21st List* (World Health Organization, 2019).
6. W. Lau, E. S. Sattely, Six enzymes from mayapple that complete the biosynthetic pathway to the etoposide aglycone. *Science* **349**, 1224–1228 (2015).
7. J. Li, X. Zhang, H. Renata, Asymmetric chemoenzymatic synthesis of (-)-podophyllotoxin and related aryltetralin lignans. *Angew. Chem. Int. Ed. Engl.* **58**, 11657–11660 (2019).
8. M. Lazzarotto *et al.*, Chemoenzymatic total synthesis of deoxy-, epi-, and podophyllotoxin and a biocatalytic kinetic resolution of dibenzylbutyrolactones. *Angew. Chem. Int. Ed. Engl.* **58**, 8226–8230 (2019).
9. W. C. Chang, Z. J. Yang, Y. H. Tu, T. C. Chien, Reaction mechanism of a nonheme iron enzyme catalyzed oxidative cyclization via C-C bond formation. *Org. Lett.* **21**, 228–232 (2019).
10. M. C. Tang, Y. Zou, K. Watanabe, C. T. Walsh, Y. Tang, Oxidative cyclization in natural product biosynthesis. *Chem. Rev.* **117**, 5226–5333 (2017).
11. J. R. Chekan *et al.*, Scalable biosynthesis of the seaweed neurochemical, kainic acid. *Angew. Chem. Int. Ed. Engl.* **58**, 8454–8457 (2019).
12. K. Dornevil *et al.*, Cross-linking of dicyclotyrosine by the cytochrome P450 enzyme CYP121 from *Mycobacterium tuberculosis* proceeds through a catalytic shunt pathway. *J. Biol. Chem.* **292**, 13645–13657 (2017).
13. O. K. Park, H. Y. Choi, G. W. Kim, W. G. Kim, Generation of new complestatin analogues by heterologous expression of the complestatin biosynthetic gene cluster from *Streptomyces chartreusis* AN1542. *ChemBioChem* **17**, 1725–1731 (2016).
14. T. Spolitak, D. P. Ballou, Evidence for catalytic intermediates involved in generating the chromopyrrolic acid scaffold of rebeccamycin by RebO and RebD. *Arch. Biochem. Biophys.* **573**, 111–119 (2015).
15. P. Belin *et al.*, Identification and structural basis of the reaction catalyzed by CYP121, an essential cytochrome P450 in *Mycobacterium tuberculosis*. *Proc. Natl. Acad. Sci. U.S.A.* **106**, 7426–7431 (2009).
16. T. Nishizawa, S. Grüschow, D. H. Jayamaha, C. Nishizawa-Harada, D. H. Sherman, Enzymatic assembly of the bis-indole core of rebeccamycin. *J. Am. Chem. Soc.* **128**, 724–725 (2006).
17. H. T. Chiu *et al.*, Molecular cloning and sequence analysis of the complestatin biosynthetic gene cluster. *Proc. Natl. Acad. Sci. U.S.A.* **98**, 8548–8553 (2001).
18. M. S. Islam, T. M. Leissing, R. Chowdhury, R. J. Hopkinson, C. J. Schofield, 2-oxoglutarate-dependent oxygenases. *Annu. Rev. Biochem.* **87**, 585–620 (2018).
19. Z. Zhang *et al.*, Crystal structure of a clavaminate synthase-Fe(II)-2-oxoglutarate-substrate-NO complex: Evidence for metal centered rearrangements. *FEBS Lett.* **517**, 7–12 (2002).
20. R. P. Hausinger, FeII/alpha-ketoglutarate-dependent hydroxylases and related enzymes. *Crit. Rev. Biochem. Mol. Biol.* **39**, 21–68 (2004).
21. M. A. McDonough, C. Loenarz, R. Chowdhury, I. J. Clifton, C. J. Schofield, Structural studies on human 2-oxoglutarate dependent oxygenases. *Curr. Opin. Struct. Biol.* **20**, 659–672 (2010).
22. S. D. Wong *et al.*, Elucidation of the Fe(IV)=O intermediate in the catalytic cycle of the halogenase SyrB2. *Nature* **499**, 320–323 (2013).
23. A. J. Mitchell *et al.*, Structural basis for halogenation by iron- and 2-oxo-glutarate-dependent enzyme WelO5. *Nat. Chem. Biol.* **12**, 636–640 (2016).
24. P. Emsley, B. Lohkamp, W. G. Scott, K. Cowtan, Features and development of Coot. *Acta Crystallogr. D Biol. Crystallogr.* **66**, 486–501 (2010).
25. M. Kuhn, A. Wartburg, Podophyllum-Lignane - Struktur Und Absolutkonfiguration Von Podorhizol-Beta-D-Glucosid ([Lignan F). 19. Mitt Uber Mitosehemmende Naturstoffe. *Helv. Chim. Acta* **50**, 1546–1565 (1967).
26. A. S. Feliciano *et al.*, Lignans from *Juniperus thurifera*. *Phytochemistry* **28**, 2863–2866 (1989).
27. M. L. Matthews *et al.*, Substrate positioning controls the partition between halogenation and hydroxylation in the aliphatic halogenase, SyrB2. *Proc. Natl. Acad. Sci. U.S.A.* **106**, 17723–17728 (2009).
28. H. J. Kulik, C. L. Drennan, Substrate placement influences reactivity in non-heme Fe(II) halogenases and hydroxylases. *J. Biol. Chem.* **288**, 11233–11241 (2013).
29. M. E. Neugebauer *et al.*, A family of radical halogenases for the engineering of amino-acid-based products. *Nat. Chem. Biol.* **15**, 1009–1016 (2019).
30. R. Mehmood, V. Vennelakanti, H. J. Kulik, Spectroscopically guided simulations reveal distinct strategies for positioning substrates to achieve selectivity in non-heme Fe(II)/α-ketoglutarate-dependent halogenases. *ACS Catal.* **11**, 12394–12408 (2021).

31. J. W. Bode, M. P. Doyle, M. N. Protopopova, Q. L. Zhou, Intramolecular regioselective insertion into unactivated prochiral carbon-hydrogen bonds with diazoacetates of primary alcohols catalyzed by chiral dirhodium(II) carboxamidates. Highly enantioselective total synthesis of natural lignan lactones. *J. Org. Chem.* **61**, 9146–9155 (1996).
32. T. Itoh, J. Chika, Y. Takagi, S. Nishiyama, An efficient enantioselective total synthesis of antitumor lignans - Synthesis of enantiomerically pure 4-hydroxyalkanenitriles via an enzymatic-reaction. *J. Org. Chem.* **58**, 5717–5723 (1993).
33. A. Pelter, R. S. Ward, M. C. Pritchard, I. T. Kay, A short versatile synthesis of aryltetralin lignans including deoxyisopodophyllotoxin and epi-isopodophyllotoxin. *J. Chem. Soc., Perkin Trans. 1* **6**, 1615–1623 (1988).
34. R. C. Cambie, P. A. Craw, P. S. Rutledge, P. D. Woodgate, Oxidative coupling of lignans. 3. Non-phenolic oxidative coupling of deoxypodorhizon and related-compounds. *Aust. J. Chem.* **41**, 897–918 (1988).
35. J. L. Grant, M. E. Mitchell, T. M. Makris, Catalytic strategy for carbon-carbon bond scission by the cytochrome P450 OleT. *Proc. Natl. Acad. Sci. U.S.A.* **113**, 10049–10054 (2016).
36. C. P. Yu *et al.*, Elucidating the reaction pathway of decarboxylation-assisted olefination catalyzed by a mononuclear non-heme iron enzyme. *J. Am. Chem. Soc.* **140**, 15190–15193 (2018).
37. S. Martinez, R. P. Hausinger, Catalytic mechanisms of Fe(II)- and 2-oxoglutarate-dependent oxygenases. *J. Biol. Chem.* **290**, 20702–20711 (2015).
38. S. S. Gao, N. Naowarojna, R. Cheng, X. Liu, P. Liu, Recent examples of α-ketoglutarate-dependent mononuclear non-haem iron enzymes in natural product biosyntheses. *Nat. Prod. Rep.* **35**, 792–837 (2018).
39. P. Rabe, J. J. A. G. Kamps, C. J. Schofield, C. T. Lohans, Roles of 2-oxoglutarate oxygenases and isopenicillin N synthase in β-lactam biosynthesis. *Nat. Prod. Rep.* **35**, 735–756 (2018).
40. H. Nakamura, Y. Matsuda, I. Abe, Unique chemistry of non-heme iron enzymes in fungal biosynthetic pathways. *Nat. Prod. Rep.* **35**, 633–645 (2018).
41. T. Y. Chen *et al.*, Pathway from N-alkylglycine to alkylisonitrile catalyzed by iron(II) and 2-oxoglutarate-dependent oxygenases. *Angew. Chem. Int. Ed. Engl.* **59**, 7367–7371 (2020).
42. N. P. Dunham *et al.*, Hydrogen donation but not abstraction by a tyrosine (Y68) during endoperoxide installation by verruculogen synthase (FtmOx1). *J. Am. Chem. Soc.* **141**, 9964–9979 (2019).
43. N. C. Harris *et al.*, Isonitrile formation by a non-heme iron(II)-dependent oxidase/decarboxylase. *Angew. Chem. Int. Ed. Engl.* **57**, 9707–9710 (2018).
44. N. Ishikawa *et al.*, Non-heme dioxygenase catalyzes atypical oxidations of 6,7-bicyclic systems to form the 6,6-quinolone core of viridicatin-type fungal alkaloids. *Angew. Chem. Int. Ed. Engl.* **53**, 12880–12884 (2014).
45. W. C. Chang *et al.*, Mechanism of the C5 stereoinversion reaction in the biosynthesis of carbapenem antibiotics. *Science* **343**, 1140–1144 (2014).
46. A. R. Balo *et al.*, Trapping a cross-linked lysine-tryptophan radical in the catalytic cycle of the radical SAM enzyme SuiB. *Proc. Natl. Acad. Sci. U.S.A.* **118**, e2101571118 (2021).